Production of Aluminium and the Heavy Magnesium Isotopes in Asymptotic Giant Branch Stars

A. I. Karakas and J. C. Lattanzio

School of Mathematical Sciences, Monash University, Wellington Road, Clayton, Vic 3800, Australia
amanda.karakas@maths.monash.edu.au

Abstract: We investigate the production of aluminium and magnesium in asymptotic giant branch models covering a wide range in mass and composition. We evolve models from the pre-main sequence, through all intermediate stages, to near the end of the thermally-pulsing asymptotic giant branch phase. We then perform detailed nucleosynthesis calculations from which we determine the production of the magnesium and aluminium isotopes as a function of the stellar mass and composition. We present the stellar yields of sodium and the magnesium and aluminium isotopes. We discuss the abundance predictions from the stellar models in reference to abundance anomalies observed in globular cluster stars.

Keywords: stars: AGB and post-AGB — stars: abundances — stars: interiors — stars: low mass — ISM: abundances

1 Introduction

In recent years our attempts to understand many aspects of nucleosynthesis and stellar evolution have come to rely on our understanding of the production of the magnesium and aluminium isotopes. For example, abundance anomalies in globular cluster stars have been a problem for many years, and the role of Mg and Al is central, and far from understood (Shetrone 1996; Yong et al. 2003). At the heart of this problem is the quest for the origin of the Mg and Al anomalies: are they produced in the star itself, and mixed to the surface by some form of deep mixing (Denissenkov & Weiss 1996), or are they the result of pollution from an earlier generation of stars? The latter would seem to implicate asymptotic giant branch (AGB) stars (Denissenkov et al. 1998; Ventura et al. 2001), where Mg and Al can be produced by thermal pulses (and mixed into the envelope by the subsequent third dredge-up, hereafter TDU) and hot bottom burning (HBB). For a review of the AGB phase of evolution we refer the reader to Iben Jr (1991), Frost & Lattanzio (1996), and Busso, Gallino, & Wasserburg (1999).

Although all isotopes of magnesium are produced by massive stars, low-metallicity supernovae models mostly produce ^{24}Mg, with very little ^{25}Mg and ^{26}Mg synthesised. Only when the initial metallicity of the model reaches about [Fe/H] ~ -1 is there substantial ^{25}Mg and ^{26}Mg production (Fenner et al. 2003). Observations of the Mg isotopic ratios in metal-poor stars (Gay & Lambert 2000) show that there is more of the neutron-rich Mg isotopes in these stars than expected from detailed chemical evolution models using supernovae yields alone (Timmes, Woosley, & Weaver 1995). Other possible sources of the neutron-rich magnesium isotopes include the winds from Wolf-Rayet (WR) (Maeder 1983; Woosley, Langer, & Weaver 1995) and AGB stars (Forestini & Charbonnel

1997; Siess, Livio, & Lattanzio 2002). There are currently no quantitative studies of the production of the neutron-rich Mg isotopes in low-metallicity WR stars. There are quantitative studies of magnesium production in low-metallicity AGB stars (Forestini & Charbonnel 1997; Siess et al. 2002) but these studies do not cover a sufficiently large range of mass or composition to produce yields suitable for galactic chemical evolution models. Further, the yields of Forestini & Charbonnel (1997) involved extrapolations from parameterised 'synthetic' models, rather than being the result of detailed stellar evolutionary calculations. For this reason, a quantitative estimate of the production of the neutron-rich Mg isotopes from AGB models of different mass and metallicity is the main aim of this paper.

Magnesium is processed together with aluminium through the Mg–Al chain, and hence a discussion of one requires a discussion of the other. The main product of the Mg–Al chain is the unstable ^{26}Al, which has a half-life of $\tau_{1/2} = 710,000$ years. The decay of ^{26}Al into ^{26}Mg results in the emission of 1.809 MeV photons, which can be used to probe the spatial distribution of the stars responsible for the ^{26}Al production (Chen, Gehrels, & Diehls 1995). The COMPTEL satellite mapped the distribution of ^{26}Al in the Galaxy, and the future INTEGRAL satellite will reveal details of that map (Prantzos 1998). Whilst most of the ^{26}Al observed in the Galaxy today probably originated in young massive WR stars (Prantzos 1993), contributions from other sources such as classical novae (José & Hernanz 1998) and low and intermediate mass AGB stars might be important (Meynet 1994). The production and destruction of ^{26}Al in AGB stars has been discussed in detail by Mowlavi & Meynet (2000). These authors found that HBB in massive AGB stars could be an important source of ^{26}Al. Nollett, Busso, & Wasserburg (2003)

recently studied parameterised extra-mixing processes in low mass[1] AGB models. They found that, depending on the mixing parameters used, ^{26}Al can be produced in sufficient amounts to explain the ^{26}Al/^{27}Al ratio inferred to have been present in some circumstellar oxide grains at the time of their formation.

In this paper we present detailed stellar models for a wide range of masses and compositions, evolved from the pre-main sequence to near the end of the thermally-pulsing AGB phase. We discuss the production and destruction mechanisms for the Mg and Al isotopes, and provide yields suitable for chemical evolution calculations. We also present yields for sodium as there are currently no yields for this element from low to intermediate mass stars published in the literature.

In the next section we discuss the stellar models used to investigate the production of Mg and Al. In the third section we discuss the site of Mg and Al production in AGB stars, giving examples from stellar models of different masses and compositions. We present our yields for ^{23}Na, ^{24}Mg, ^{25}Mg, ^{26}Mg, ^{26}Al, and ^{27}Al in Section 4. We finish with a discussion of the main applications of the results presented.

2 Stellar Models

Models were calculated with the Mount Stromlo Stellar Structure code, updated to include the OPAL opacities of Iglesias & Rogers (1996). We discuss the details of the code used and the initial abundances in Frost & Lattanzio (1996) and Karakas, Lattanzio, & Pols (2002). The reader is also referred to Wood & Zarro (1981) and Lattanzio (1986). Mass loss was included using the prescription of Vassiliadis & Wood (1993) but without the modification for M greater than 2.5M$_\odot$. We calculated model sequences for three different initial compositions: $Z = 0.02$, 0.008, and 0.004, over a range in mass $1 \le M_0$ (M$_\odot$) ≤ 6 where M_0 is the initial stellar mass.

Initial abundances for the solar composition ($Z = 0.02$) models were taken from Grevesse, Noels, & Sauval (1992), and the initial Large Magellanic Cloud compositions ($Z = 0.008$) and Small Magellanic Cloud compositions ($Z = 0.004$) were from Russell & Dopita (1992). In the evolutionary models we include six species: H, ^{3}He, ^{4}He, ^{12}C, ^{14}N, and ^{16}O, and we present the initial abundances (in mass fractions) in Table 1. Note that we set ^{3}He $= 0$ initially. We use the standard mixing-length theory for convection, with a mixing-length parameter $\alpha = l/H_P = 1.75$. We do not include convective overshoot in our models even though there is evidence that it may be important on the main sequence for intermediate mass stars (Chiosi et al. 1989; Schaller et al. 1992). The latest models suggest that the amount of overshooting required is small (Barmina, Girardi, & Chiosi 2002), and for simplicity we have ignored overshoot in the models to be presented. We included semiconvection during core

[1]Hereafter low mass refers to models with $M \le 2.25$ M$_\odot$ and intermediate mass refers to models with $M > 2.25$ M$_\odot$.

Table 1. Initial compositions (in mass fractions) used for the stellar models

	$Z = 0.02$ Solar	$Z = 0.008$ LMC	$Z = 0.004$ SMC
X	0.6872	0.7369	0.7484
Y	0.2928	0.2551	0.2476
^{12}C	3.4080E$-$3	9.6959E$-$4	4.8229E$-$4
^{14}N	1.0542E$-$3	1.4240E$-$4	4.4695E$-$5
^{16}O	9.6000E$-$3	2.6395E$-$3	1.2830E$-$3
Other Z	5.9378E$-$3	4.2484E$-$3	2.1899E$-$3

He burning using the prescription described in Lattanzio (1986). We find the convective boundary at the base of the outer envelope by searching for a neutral border to the convective zone, in the manner described in Frost & Lattanzio (1996) and Karakas et al. (2002). We note that this method does increase the efficiency of the TDU for low-mass models but we do not find any dredge-up for the $Z = 0.02$ models with $M \le 2.0$M$_\odot$. Reaction rates used in the evolution code were taken mostly from Caughlan & Fowler (1988), but with updates included in the nucleosynthesis calculations (see below).

We performed detailed nucleosynthesis calculations separately using a post-processing nucleosynthesis code which includes time-dependent mixing in all convective zones. In the nucleosynthesis network there are 74 nuclear species: from neutrons and protons up to sulphur there are 59 nuclei, with another 14 iron group species to allow neutron capture on iron seed nuclei. There is also an additional 'particle' g which has the function of counting the number of neutron captures occurring beyond ^{60}Ni. The reaction network is terminated by a neutron capture on ^{61}Ni followed by an *ad hoc* decay, producing the particle represented by the symbol g: ^{61}Ni(n, γ)^{62}Ni $\rightarrow$ ^{61}Ni $+ g$. Following the method of Jorissen & Arnould (1989), neutron captures on the missing nuclides are modelled by neutron sinks, meaning that the ^{34}S(n, γ)^{35}S and the ^{61}Ni(n, γ)^{62}Ni reactions are given some averaged cross section values in order to represent all nuclei from ^{34}S to ^{54}Fe and from ^{61}Ni to ^{209}Bi respectively. The initial abundances for H, ^{4}He, ^{12}C, ^{14}N, and ^{16}O are the same as used in the evolution code (Table 1); all other species are either solar or scaled solar (see Table 5).

The bulk of the 506 reaction rates are from the Reaclib Data Tables, based on the 1991 updated version of the compilation by Thielemann, Arnould, & Truran (1991). We include recent reaction rates for α, proton, and neutron capture reactions when available, as detailed in Lugaro (1998, 2001).

3 Production of Magnesium in AGB Stars

The magnesium and aluminium isotopes are produced in three sites in AGB stars: the hydrogen-burning shell (H shell) via the Mg–Al chain, the helium-burning shell (He shell) via α-capture on ^{22}Ne, and at the base of the convective envelope in the most massive AGB stars that
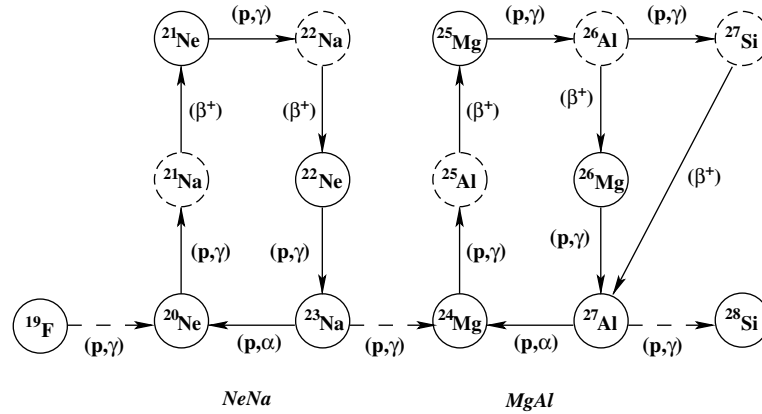
Figure 1 Reactions of the Ne–Na and Mg–Al chains. Unstable isotopes are denoted by dashed circles (Rolfs & Rodney 1988; Arnould et al. 1999).

experience HBB, again via the Mg–Al chain. The efficiency of production of each site depends in a complicated way on the temperature (i.e. initial mass), initial composition, and the extent to which each site affects the other.

In this section, we discuss the effects and efficiency of each production site, giving examples from our extensive set of stellar models. We try to separate out the effects of the H-burning shell, He-burning shell, and HBB using appropriate models, but note that in the most massive models this is quite difficult.

3.1 Hydrogen-Burning Shell

Magnesium and aluminium are produced in the H-burning shell via the activation of the Mg–Al chain, which begins operation at temperatures of about 30×10^6 K (Arnould, Goriely, & Jorissen 1999). This involves the radioactive nuclide ^{26}Al, which has a ground state ^{26}Al$_g$ that has to be considered a separate species from the short-lived ($\tau_{1/2} = 6.35$ s) isomeric state ^{26}Al$_m$, since they are out of thermal equilibrium at the relevant temperatures (Arnould et al. 1999). Hereafter, when we refer to ^{26}Al we are referring to the ground state, ^{26}Al$_g$. In Figure 1 we show the reactions involved in the Ne–Na and the Mg–Al chains (Arnould et al. 1999; Rolfs & Rodney 1988). The first isotope in the Mg–Al chain to be effected is ^{25}Mg, which is burnt to ^{26}Al. The lifetime of β-decay relative to proton capture generally favours proton capture within the H-burning shell. This produces the unstable ^{27}Si which β-decays (with a lifetime on the order of a few seconds) to ^{27}Al. The rate of ^{26}Mg + p is slow until the temperature reaches about 60×10^6 K, so we only find small reductions in ^{26}Mg in most AGB models. We note that the abundance of ^{26}Mg is enhanced by the decay of ^{26}Al in the H-shell ashes. Proton capture on ^{24}Mg requires higher temperatures than those required for the other reactions in the Mg–Al chain. For that reason most of our models show little change in the abundance of this isotope due to the slow rate of proton capture at temperatures below about 70×10^6 K.

The main effect of the Ne–Na chain is the production of ^{23}Na from proton capture on ^{22}Ne, which begins at about 20×10^6 K (Arnould et al. 1999). The rare neon isotope, ^{21}Ne, can be substantially enhanced by an unnoticeable destruction of ^{20}Ne at temperatures below 40×10^6 K, but at temperatures above this ^{21}Ne is completely destroyed. ^{20}Ne can be slightly destroyed at temperatures above 50×10^6 K, but the destruction of ^{23}Na at temperatures over about 80×10^6 K can lead to a slight enhancement in the ^{20}Ne abundance (Arnould et al. 1999).

The lowest temperature in the H-burning shells of our AGB models is just over 40×10^6 K for the $1 \, M_\odot$, $Z = 0.02$ model, and the highest temperatures reached are about 98×10^6 K for the $6 \, M_\odot$, $Z = 0.004$ model. Thus even in the lowest mass models the Mg–Al chain is active, depleting ^{25}Mg and producing ^{26}Al. However we still need the operation of the TDU to mix the products of the H shell to the surface. We only find the TDU in models with $M > 2 M_\odot$ at solar composition, and for less massive models there are no surface abundance changes during the thermally-pulsing AGB (TP–AGB) phase. For the Large Magellanic Cloud (with $Z = 0.008$) and Small Magellanic Cloud (with $Z = 0.004$) models, there is substantial dredge-up at $1.5 M_\odot$, enough to turn the models into carbon stars, but no dredge-up for either composition at $1.25 \, M_\odot$.

In the low-mass models, the change to the surface abundance of the Na, Mg, and Al isotopes with efficient TDU is as follows. There is a very small depletion in the abundance of ^{25}Mg and a slight increase in ^{26}Mg, ^{26}Al, and ^{27}Al. The ^{24}Mg abundance remains unchanged. The ^{23}Na abundance increases after each dredge-up episode, but the increase over the entire TP–AGB phase is small compared to the increase observed in models with HBB. We demonstrate the effect of H-burning nucleosynthesis in Figure 2. In the left panel of Figure 2 we show the composition profile of the $1.5 \, M_\odot$, $Z = 0.004$ model just before the 14th thermal pulse, showing the ashes of the H-burning shell. The shaded region denotes the convective envelope. The maximum extent of the convective pocket
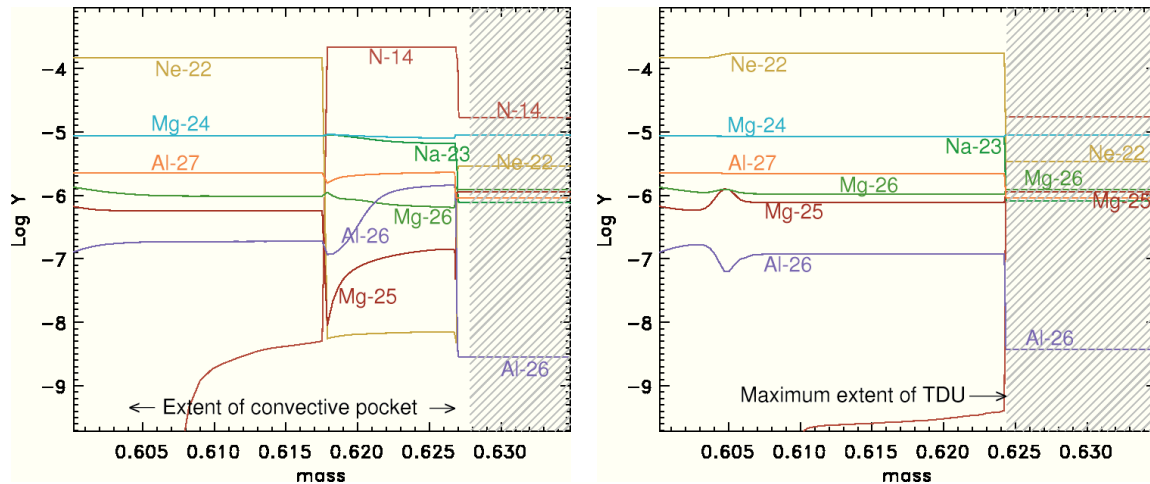
Figure 2   Composition profile for the 1.5 $M_\odot$, $Z = 0.004$ model just before the 14th thermal pulse (*left*), and at the maximum extent of the following dredge-up episode (*right*).
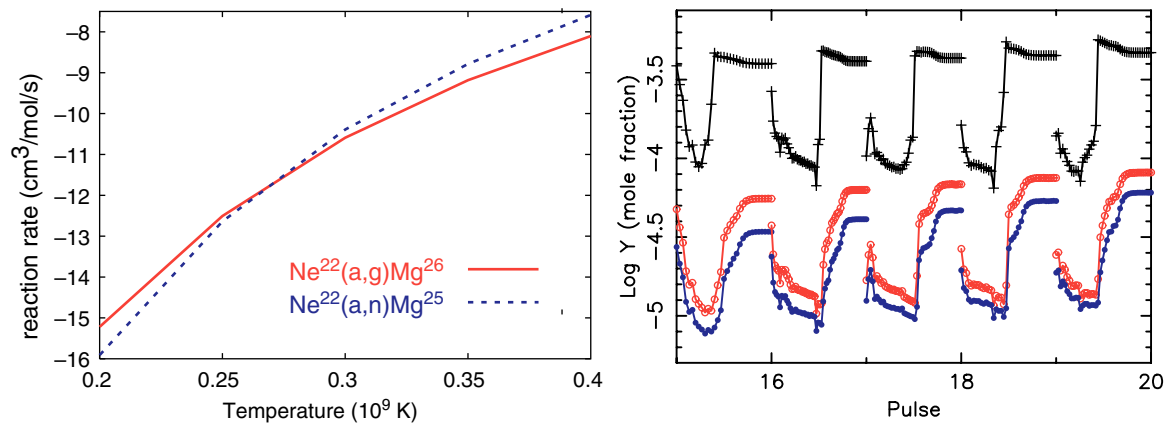
Figure 3   (*left*) The ^{22}Ne$(\alpha, n)^{25}$Mg and ^{22}Ne$(\alpha, \gamma)^{26}$Mg reaction rates as a function of the temperature. (*right*) The intershell abundances ^{22}Ne (black plus signs), ^{25}Mg (red open circles), and ^{26}Mg (blue closed circles) as a function of pulse number for the 4 $M_\odot$, $Z = 0.008$ model. In this diagram we plot the intershell abundances for the 15th to the 20th pulse, but only during the time when the convective shell is present; the x-axis is the (scaled) duration of the convective pocket.

during the 14th thermal pulse is noted. In the right panel of Figure 2 we show the composition profile at the maximum extent of the TDU, after the pulse. The composition of ^{26}Al in the intershell has been homogenised by the convective pocket, but is not destroyed by neutron capture. After the next dredge-up episode, the surface abundance of ^{26}Al has increased by about 30%.

In conclusion, the operation of the H shell in low-mass models is quantitatively unimportant to the production of the Mg isotopes. Some ^{23}Na and ^{26}Al is produced in low mass, low-metallicity AGB models, but this conclusion suffers from many uncertainties. In the next two sections we discuss the operation of the He-burning shell and HBB, and show that these sites are much more important in intermediate mass AGB models than the H-burning shell.

3.2 Helium-Burning Shell

The He-burning shell in AGB stars is a rich source of nucleosynthesis. The main result is the production of ^{12}C, which when mixed to the surface may produce carbon stars.

There is also a wealth of other He-burning products such as ^{22}Ne, ^{25}Mg, and ^{26}Mg, plus species produced through the combined operation of the H and He-burning shells such as ^{19}F (Forestini et al. 1992) and ^{23}Na (Mowlavi 1999b).

Substantial ^{22}Ne is created during a thermal pulse by α-capture onto the ^{14}N left by the H-burning shell during the preceding interpulse period. If the temperature exceeds about 300×10^6 K, ^{25}Mg and ^{26}Mg can be produced in substantial quantities by α-capture onto ^{22}Ne via the reactions ^{22}Ne$(\alpha,n)^{25}$Mg and ^{22}Ne$(\alpha, \gamma)^{26}$Mg. In the right panel of Figure 3 we show the time variation of the intershell abundances of ^{22}Ne, ^{25}Mg, and ^{26}Mg for the 4 $M_\odot$, $Z = 0.008$ model for the 15th to the 20th pulse. This model experiences very deep dredge-up, which began following the third thermal pulse. The abundance for each species initially decreases due to the growth of the convective shell into the region previously processed by the H shell. At the end of the preceding interpulse phase this region has been depleted in ^{22}Ne, ^{25}Mg, and ^{26}Mg via H burning at temperatures near 80×10^6 K. As the temperature
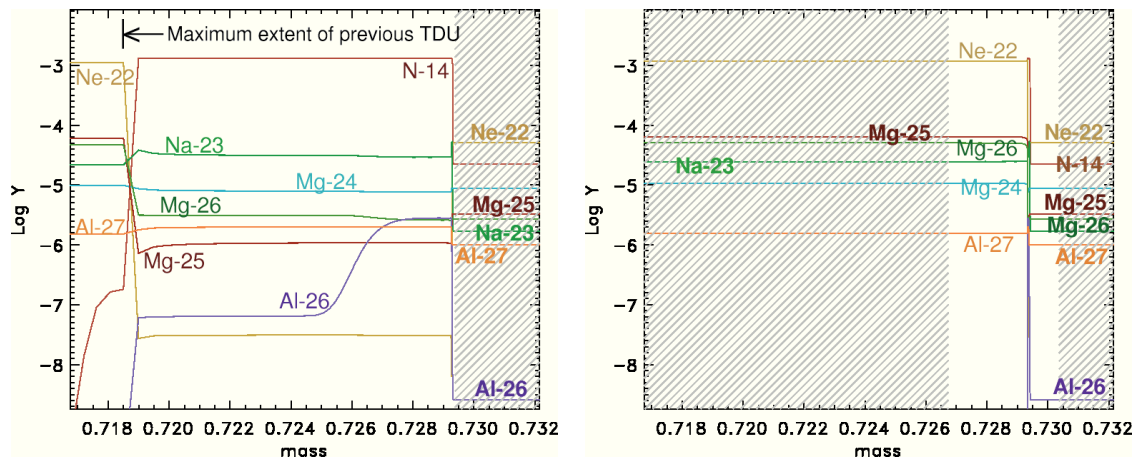
Figure 4 Composition profile against interior mass for the $3\,M_\odot$, $Z = 0.004$ model. Shaded regions are convective. (*left*) Just before the 23rd thermal pulse. (*right*) During the 23rd thermal pulse, showing substantial ^{22}Ne, ^{25}Mg, and ^{26}Mg production. The maximum temperature in the He shell was just over 330×10^6 K.

in the intershell convective region increases, successive α-captures onto ^{14}N first produce an increase in the ^{22}Ne abundance followed by an increase in ^{25}Mg and ^{26}Mg when the temperature reaches $\sim 300 \times 10^6$ K. Note that after the intershell convective pulse dies down, the final ^{22}Ne abundance is still high, making it the third most abundant species in this region (after ^{4}He and ^{12}C, but higher than ^{16}O).

The exact amounts of ^{25}Mg and ^{26}Mg produced in the He shell are dependent on the reaction rates. In the left-hand panel of Figure 3 we plot the NACRE reaction rates (Angulo et al. 1999) for the two ^{22}Ne α-capture reactions at the relevant temperatures for He-shell burning. The ^{22}Ne(α,n)^{25}Mg reaction is slightly faster, favouring production of ^{25}Mg over ^{26}Mg. At the highest temperatures reached in the He shell, around 380×10^6 K for the most massive AGB stars, the rate for the ^{22}Ne(α,n)^{25}Mg reaction is almost an order of magnitude faster than the ^{22}Ne(α, γ)^{26}Mg reaction rate (see Figure 3).

The relative amount of ^{25}Mg to ^{26}Mg produced in the He shell is also dependent on the other nuclear burning sites: in the hottest H shells, ^{25}Mg can be substantially depleted compared to ^{26}Mg. Because the ashes of the H-burning shell are engulfed by the next thermal pulse, the pre-pulse abundance of the two heavy Mg isotopes can be quite different. For example, in the $6\,M_\odot$, $Z = 0.004$ model, the abundance of ^{25}Mg/^{26}Mg can be as low as 0.2 at the beginning of a thermal pulse (c.f. the initial ratio ^{25}Mg/^{26}Mg ~ 0.9). For this model, even though the temperature in the He shell favours the production of ^{25}Mg over ^{26}Mg, the ratio ^{25}Mg/^{26}Mg ~ 0.65 just prior to the TDU.

Temperatures exceed 300×10^6 K in the He shell of models with $M \gtrsim 3\,M_\odot$, depending on the composition. For example, the $3\,M_\odot$ solar composition model does not reach temperatures of 300×10^6 K in the He shell until the very last calculated thermal pulse, but the temperature in the He shell of the $3\,M_\odot$, $Z = 0.004$ model exceeds 300×10^6 K after the 8th thermal pulse. In Figure 4 we

show the composition profile for the $3\,M_\odot$, $Z = 0.004$ model just prior (left panel) and during (right panel) the 23rd thermal pulse. This model began dredge-up after the second thermal pulse and soon developed very deep dredge-up. This diagram demonstrates the large increase in the ^{25}Mg and ^{26}Mg abundances in the intershell when the temperature exceeds 300×10^6 K.

In conclusion, the He shell is the most important production site of the heavy magnesium isotopes but depends in a complicated way on the temperatures in the He shell and the abundance of the matter left by the H shell at the end of the interpulse phase. The aluminium isotopes are not produced in the He shell. The isotope ^{26}Al can be depleted by neutron capture by the reactions ^{26}Al(n,p)^{26}Mg and ^{26}Al(n,α)^{23}Na, noting that neutrons come from the ^{22}Ne(α,n)^{25}Mg reaction. The isotope ^{27}Al is not altered at the temperatures found in the He shells of AGB stars.

3.3 Hot Bottom Burning in Massive AGB Stars

For AGB models with $M \gtrsim 4\,M_\odot$, depending on the composition, the bottom of the convective envelope reaches into the top of the H-burning shell. H burning occurs primarily via the CNO cycle, but also via the Ne–Na and Mg–Al chains if the temperature is high enough. This site then becomes important for the production of many elements, including nitrogen (Frost et al. 1998; Chieffi et al. 2001), lithium (Travaglio et al. 2001), and sodium (Mowlavi 1999b), as well as magnesium and aluminium (Mowlavi & Meynet 2000).

The region in the envelope that is hot enough for H burning is quite thin but owing to efficient mixing, where the convective turnover time scale is of the order of one year, the matter in the entire envelope passes through the hot region at least 1000 times during every thermal pulse cycle. This means that the CN cycle operates in equilibrium after a few interpulse periods, reducing the ^{12}C/^{13}C ratio from the pre-AGB value near 20 to the equilibrium value of about four. Hot bottom burning also prevents
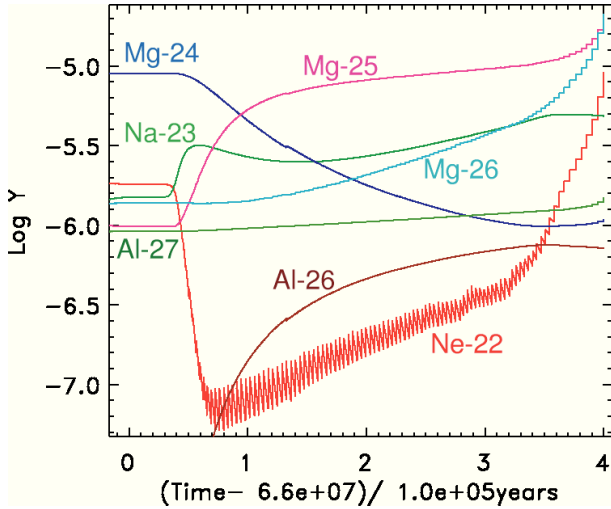
Figure 5 Surface abundance evolution during the AGB stage of the neon, sodium, and magnesium isotopes for the $6M_\odot$, $Z = 0.004$ model.

carbon star formation (Boothroyd, Sackmann, & Ahern 1993), because the ^{12}C mixed into the envelope by the TDU is burnt mostly to ^{14}N. There are also depletions in ^{15}N, ^{18}O, and, if the temperature is high enough, ^{16}O.

When the temperature is high enough for the Ne–Na and Mg–Al chains to operate,[2] ^{23}Na and ^{26}Al are produced at the expense of ^{22}Ne and ^{25}Mg. The Ne–Na and Mg–Al chains follow the same sequence as seen in the H shell, except that temperatures of at least $\sim 90 \times 10^6$ K are required before ^{24}Mg is substantially depleted. In Figure 5 we show the time variation of various surface abundances for the $6\,M_\odot$, $Z = 0.004$ model. This figure demonstrates the most extreme behaviour we found in the HBB models, with temperatures exceeding 94×10^6 K at the base of the convective envelope. Large depletions in ^{16}O, ^{24}Mg, and ^{22}Ne are followed by significant enhancements in ^{25}Mg, ^{26}Mg, and ^{26}Al. We also observe moderate enhancements in ^{23}Na and ^{27}Al. After the mass of the envelope is reduced below about $2\,M_\odot$, the temperature is too low for HBB and the continuation of dredge-up turns the model into an obscured carbon star, with C/O ≥ 1 (see Frost et al. 1998).

4 Stellar Yields

Low to intermediate mass stars are important for galactic chemical evolution for at least three reasons: (1) their rich nucleosynthesis; (2) their high mass-loss rates during the first and asymptotic giant branch phases; (3) their high frequency compared to more massive stars.

We define a stellar yield in the same way as Marigo (2001):

$$M_k = \int_0^\tau [X(k) - X_0(k)] \frac{dM}{dt} dt, \qquad (1)$$

---

[2]It is higher for HBB than in the H shell, because the density is lower at the base of the convective envelope.

where M_k is the yield of species k (in solar masses), dM/dt is the current mass-loss rate, $X(k)$ and $X_0(k)$ refer to the current and initial mass fraction of species k, and τ is the total lifetime of the stellar model. The yield as defined by equation (1) can be negative, in the case where the element is destroyed, and positive if it is produced.

In practice, our models do not lose their entire envelopes during the TP–AGB evolution owing to convergence difficulties near the end of the AGB phase. For the lower masses considered, the envelope mass remaining is very small, and is less than what was lost during the last interpulse period. For example, the $1.5\,M_\odot$, $Z = 0.008$ model has a final envelope mass of $7.9 \times 10^{-2}\,M_\odot$, whereas $0.585\,M_\odot$ is lost during the last interpulse period owing to the very high mass-loss rates that develop during the VW93 superwind phase. In these cases we calculate the yield by simply removing the small remaining envelope (with its current composition). For the more massive models, there may be enough envelope mass remaining for a few thermal pulses to occur. At this stage the envelope mass is relatively small, and the effects of the TDU can be large, as the dilution is smaller. HBB has ceased by the time the model calculation ends, so we do not need to make allowance for this rather complicated process (see Izzard et al. 2003 for a recent discussion). This means that the species most affected are those which are present in the intershell convective zones. Although the surface abundances may change significantly, in most cases the yields are not dramatically altered during these last few pulses, because the amount of mass involved is small. To calculate the stellar yields in these cases we will use the principles of synthetic AGB evolution to model the few remaining pulses.

4.1 Estimating the Surface Enrichment from the Last Thermal Pulses

For each of our model sequences, we estimate the number of pulses remaining after the evolution calculation ceased. We do this by calculating the amount of matter lost from the envelope per interpulse period and the change to the mass of the H-exhausted core owing to H-shell burning and the TDU. If we assume the mass loss is constant over the interpulse period (which is approximately correct) then the amount of matter lost per interpulse is

$$\Delta M = \dot{M}(r, l, M)\tau_{ip}, \qquad (2)$$

where τ_{ip} is the interpulse period (in years) and $\dot{M}(r, l, M)$ is the mass-loss rate as a function of the radius, luminosity, and total stellar mass (in units of $M_\odot\,yr^{-1}$) taken from Vassiliadis & Wood (1993). The total mass at the ith thermal pulse is then

$$M^i = M^{i-1} - \Delta M. \qquad (3)$$

If we assume that the H-exhausted core mass grows by a constant ΔM_H per interpulse period and decreases in mass after each thermal pulse owing to the TDU, then the change in the mass of the H-exhausted core from the

Table 2. Data used to estimate the number of thermal pulses missed for each model

M_0	M_f	$M_{H,f}$	$M_{env,f}$	τ_{ip}	λ	No. TPs	Syn. TPs	TP (DU)
$Z = 0.02$								
2.0	0.77934	0.64557	0.13377	6.4448E+04	0.000	20	0	–
2.25	0.79203	0.66611	0.12592	5.5163E+05	0.234	27	0	20
2.5	1.14842	0.66260	0.48582	6.3421E+04	0.564	26	1	16
3.0	1.35827	0.68264	0.67563	5.4718E+04	0.765	25	1	9
3.5	2.04719	0.70990	1.33729	4.3107E+04	0.859	20	1	4
4.0	1.74950	0.79360	0.95590	2.3947E+04	0.975	17	2	4
5.0	2.37355	0.87447	1.49908	1.0522E+04	0.911	24	5	4
6.0	2.46296	0.92902	1.53394	6.6692E+03	0.934	37	5	4
6.5	2.47032	0.96284	1.50748	4.4233E+03	0.910	39	7	4
$Z = 0.008$								
1.9	0.86633	0.64457	0.22176	8.7680E+04	0.466	17	0	11
2.1	1.07345	0.64615	0.42730	8.9786E+04	0.638	20	0	10
2.25	1.01461	0.65275	0.36186	8.2240E+04	0.720	27	0	14
2.5	1.01177	0.66836	0.34341	8.0220E+04	0.805	27	1	10
3.0	1.24959	0.69554	0.55405	4.9568E+04	0.861	29	1	4
3.5	1.43926	0.76877	0.67049	4.0320E+04	0.969	21	1	3
4.0	1.75654	0.84163	0.91491	2.0848E+04	0.970	23	2	3
5.0	2.27375	0.88630	1.38745	1.0432E+04	0.960	58	4	2
6.0	2.14493	0.94749	1.19744	6.2960E+03	0.950	69	5	3
$Z = 0.004$								
2.25	0.96286	0.66194	0.30092	7.2128E+04	0.767	26	0	8
2.5	1.35739	0.67277	0.68462	5.8560E+04	0.817	28	0	5
3.0	1.23056	0.72634	0.50422	4.3872E+04	0.949	26	0	2
3.5	1.39107	0.81692	0.57415	2.6560E+04	0.950	23	1	2
4.0	1.63163	0.85554	0.77608	1.8192E+04	0.947	31	2	2
5.0	1.85052	0.90610	0.94442	9.3840E+03	0.952	82	3	2
6.0	1.97357	0.97854	0.99503	4.6720E+03	0.913	101	6	4

$(i-1)$th to the ith pulse is given by

$$M_H^i = M_H^{i-1} + \Delta M_H - \lambda \Delta M_H, \qquad (4)$$

where λ is the TDU efficiency parameter.[3] The detailed evolutionary sequences provide all the necessary input, i.e. from the last calculated model we take the stellar mass, H-exhausted core mass, radius, and luminosity. The quantities ΔM_H, τ_{ip}, and λ are evaluated between the last two thermal pulses. For the remaining evolution we assume that the radius, luminosity, ΔM_H, λ, and the interpulse period τ_{ip} are constant. In Table 2 we present, for the last calculated model, the stellar mass, H-exhausted core mass, envelope mass (with masses given in solar masses), the interpulse period, λ, the number of pulses calculated in detail, the number of thermal pulses calculated synthetically, and the pulse number at which the first TDU episode occurred (for models that had final envelope masses larger than $0.1\,M_\odot$). From Table 2 it is evident that only the more massive AGB models, in particular the 4, 5, and $6\,M_\odot$ models, are estimated to undergo more than one additional thermal pulse. Since the magnesium and aluminium isotopic yields are also the largest from these more massive

models, we need to estimate the contribution from these extra thermal pulses to the stellar yield calculation.

The method used to estimate the number of remaining thermal pulses can also be used to evaluate the enrichment of the envelope. We know (from the detailed nucleosynthesis calculations) the composition of the intershell for a given model. If we assume that the intershell abundances are constant for each remaining thermal pulse, we can estimate the mass of species X mixed into the envelope at a given dredge-up episode, i.e. $\Delta M_X = X_{shell} \lambda \Delta M_H$, where X_{shell} is the intershell abundance (in mass fractions). The mass fraction of species X at the surface for the ith interpulse phase will then be

$$X^i = \frac{(M_{env}^i - \lambda \Delta M_H) X^{i-1} + \Delta M_X}{M_{env}^i}, \qquad (5)$$

where X^{i-1} is the abundance of species X at the surface for the $(i-1)$th interpulse phase and M_{env}^i is the current envelope mass.

We also note the evolutionary position of the last calculated model: if at the beginning of a thermal pulse then we adjust abundances *first* before removing mass from the envelope. This was the most common situation for model calculations. Likewise, if the last calculated model

---

[3] λ is defined as the ratio of mass dredged up by the convective envelope to the amount by which the H-exhausted core mass increased during the preceding interpulse phase.

is at the beginning of an interpulse phase or some fraction from the start of the current interpulse phase, then we remove the corresponding amount of matter from the envelope before adjusting abundances. For example, for models with the last calculated model half way through the current interpulse phase, then the first calculation removes $0.5\Delta M$ from the envelope and increases the core mass by $0.5\Delta M_{\mathrm{H}}$ before adjusting abundances. Subsequent interpulse periods remove ΔM per interpulse period.
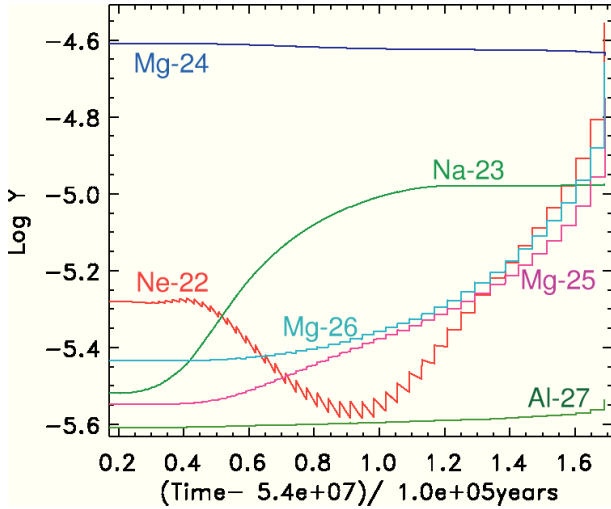
Figure 6 Surface abundance evolution during the AGB of the neon, sodium, and magnesium isotopes for the $6.5\,\mathrm{M}_\odot$, $Z = 0.02$ model. The final seven dredge-up episodes are calculated via the semi-analytic formulae described in the text.

Within the intershell, we include the magnesium and aluminium isotopes but also some other species affected by burning in the H and/or He shell: ^{4}He, ^{12}C, ^{16}O, ^{19}F, ^{22}Ne, ^{23}Na, ^{24}Mg, ^{25}Mg, ^{26}Mg, ^{26}Al, and ^{27}Al. The largest surface abundance change to the non-CNO elements is for ^{22}Ne or the heavy magnesium isotopes, depending on the mass of the model. For example, in the $4\,\mathrm{M}_\odot$, $Z = 0.008$ model (see right panel of Figure 3) only about 20% of the ^{22}Ne in the intershell is converted to Mg, whilst in the $6\,\mathrm{M}_\odot$, $Z = 0.004$ model up to 75% of the ^{22}Ne is converted to Mg. In Figure 6 we plot the surface abundances during the TP–AGB for the $6.5\,\mathrm{M}_\odot$, $Z = 0.02$ model, including the enrichment from the seven remaining thermal pulses using the method described above.

The yields, M_{k}, for the species ^{23}Na, ^{24}Mg, ^{25}Mg, ^{26}Mg, ^{26}Al, and ^{27}Al are presented in Tables 3 and 4 along with the final remnant masses. In Table 5 we present a list of the initial abundances for these isotopes used in the nucleosynthesis calculations. For models that have at least one thermal pulse remaining we present two sets of yields. The first set of yields are calculated with the λ value given in Table 2, and will be referred to as our standard set. We note however that when the envelope mass is reduced by mass loss, the efficiency of the TDU should be reduced (Straniero et al. 1997; Karakas et al. 2002), but it is unknown to what extent and at what envelope mass this effect is important. To estimate the effect of a reduced λ on the stellar yields we calculate a second set of yields with $\lambda = 0.3$ for all remaining TDU episodes.

Table 3. **Stellar yield, M_{k}, for the species ^{23}Na, ^{24}Mg, ^{25}Mg, ^{26}Mg, ^{26}Al, and ^{27}Al for the Z = 0.02 models***

M_0	M_{f}	^{23}Na	^{24}Mg	^{25}Mg	^{26}Mg	^{26}Al	^{27}Al
Z = 0.02							
1.0	0.573	1.7634E–07	6.8947E–08	6.9267E–09	1.2467E–08	2.7354E–12	7.8871E–09
1.25	0.578	5.1127E–07	1.0993E–07	8.5238E–09	2.2723E–08	2.9923E–13	1.2365E–08
1.5	0.600	1.9785E–06	1.4738E–07	1.4552E–08	2.7198E–08	5.0050E–12	1.6567E–08
1.75	0.620	5.6582E–06	1.8475E–07	2.3487E–08	2.7925E–08	5.9899E–10	2.0831E–08
1.9	0.636	8.5582E–06	2.0658E–07	2.5029E–08	3.1832E–08	1.5599E–09	2.3363E–08
2.0	0.640	1.0606E–05	2.2294E–07	2.0926E–08	3.6031E–08	5.7594E–09	2.5510E–08
2.25	0.650	1.8123E–05	2.3528E–07	−4.6726E–08	2.5237E–07	8.7344E–08	1.2475E–07
2.5	0.662	3.2015E–05	3.6554E–08	2.7225E–06	1.9633E–06	1.2106E–07	5.3593E–07
	0.664	3.1028E–05	7.0431E–08	2.2849E–06	1.7693E–06	1.2106E–07	4.9907E–07
3.0	0.682	7.6220E–05	−5.2270E–07	2.4999E–05	1.1384E–05	1.1706E–07	1.3504E–06
	0.687	7.2638E–05	−4.9197E–07	2.2072E–05	1.0211E–05	1.1708E–07	1.2952E–06
3.5	0.716	1.0496E–04	−4.3863E–06	8.7515E–05	4.0721E–05	1.1297E–07	2.2050E–06
	0.721	9.7853E–05	−4.0308E–06	7.4243E–05	3.4334E–05	1.1317E–07	2.0514E–06
4.0	0.792	7.2760E–05	−1.5926E–05	1.0841E–04	6.6976E–05	1.4430E–07	2.9603E–06
	0.800	6.9399E–05	−1.2674E–05	8.0617E–05	4.9032E–05	1.4436E–07	2.4857E–06
5.0	0.871	1.4501E–04	−3.8368E–05	2.4963E–04	2.4945E–04	4.6091E–07	1.0010E–05
	0.885	1.4109E–04	−2.8209E–05	1.5582E–04	1.5742E–04	4.6194E–07	7.7166E–06
6.0	0.929	1.0735E–03	−7.3409E–05	3.1332E–04	3.7516E–04	4.3708E–06	1.8757E–05
	0.938	1.0723E–03	−6.7917E–05	2.4499E–04	2.8340E–04	4.3735E–06	1.6769E–05
6.5	0.964	1.0069E–03	−1.0656E–04	3.6757E–04	4.3562E–04	5.0231E–06	1.8744E–05
	0.972	1.0042E–03	−1.0085E–04	2.7699E–04	3.1207E–04	5.0280E–06	1.6127E–05

*Where there are two entries in the table, the first entry corresponds to the yields calculated with λ given in Table 2 and the second entry with $\lambda = 0.3$.

Table 4. Same as for Table 3, except for the $Z = 0.008$ and $Z = 0.004$ models

M_0	M_{f}	^{23}Na	^{24}Mg	^{25}Mg	^{26}Mg	^{26}Al	^{27}Al
$Z = 0.008$							
1.0	0.598	4.1535E–07	4.5824E–08	−1.6742E–08	2.8616E–08	1.6790E–09	5.4133E–09
1.25	0.610	9.7129E–07	7.3545E–08	−2.2217E–08	4.0294E–08	3.4407E–09	8.6075E–09
1.5	0.630	3.6258E–06	8.5740E–08	−1.0535E–07	3.1920E–08	5.7168E–08	9.2714E–08
1.75	0.640	1.1853E–05	7.0984E–08	−3.9331E–07	9.7418E–08	1.1946E–07	5.1726E–07
1.9	0.640	1.7225E–05	7.1013E–09	−2.9855E–07	1.4747E–07	1.3459E–07	8.4026E–07
2.1	0.650	2.9273E–05	−9.8662E–08	7.7372E–07	8.6305E–07	1.4331E–07	1.4170E–06
2.25	0.650	4.2156E–05	−2.1077E–07	3.3402E–06	2.0867E–06	1.3154E–07	1.9465E–06
2.5	0.663	7.0590E–05	−6.0006E–07	1.6685E–05	7.5526E–06	1.1130E–07	2.7638E–06
	0.668	6.7914E–05	−6.1339E–07	1.5179E–05	6.9610E–06	1.1121E–07	2.7100E–06
3.0	0.695	1.5945E–04	−1.3435E–06	1.1521E–04	5.5123E–05	1.1593E–07	5.1229E–06
	0.701	1.4943E–04	−2.2046E–06	1.0642E–04	5.0606E–05	1.1601E–07	5.0332E–06
3.5	0.766	6.4738E–05	−3.3633E–05	1.5439E–04	1.0593E–04	3.6714E–07	1.2600E–05
	0.772	6.3243E–05	−3.2304E–05	1.4011E–04	9.4812E–05	3.6715E–07	1.2271E–05
4.0	0.837	5.3055E–05	−4.0335E–05	1.8633E–04	1.5523E–04	3.4852E–07	2.5597E–05
	0.845	5.0731E–05	−3.3860E–05	1.3317E–04	1.0613E–04	3.4980E–07	2.2733E–05
5.0	0.886	1.7094E–03	−1.3715E–04	6.0703E–04	6.3009E–04	1.4136E–05	5.0051E–05
	0.898	1.7090E–03	−1.3269E–04	5.3000E–04	5.2612E–04	1.4145E–05	4.7774E–05
6.0	0.948	8.7825E–04	−7.5671E–04	1.0822E–03	5.0958E–04	4.3172E–05	3.2625E–05
	0.956	8.7837E–04	−7.5388E–04	1.0201E–03	4.1979E–04	4.3195E–05	3.0528E–05
$Z = 0.004$							
1.0	0.630	3.8845E–07	9.8444E–09	−2.9012E–08	2.8668E–08	3.1887E–09	2.6794E–09
1.25	0.640	1.0673E–06	−4.0600E–09	−7.8991E–08	4.0560E–08	3.0380E–08	5.2588E–08
1.5	0.646	3.7298E–06	−4.5635E–08	−1.9430E–07	1.5141E–08	7.0173E–08	2.7975E–07
1.75	0.650	9.3537E–06	−2.0809E–08	−2.0623E–07	8.3641E–08	6.5908E–08	6.1386E–07
1.9	0.650	1.4616E–05	−1.0467E–06	2.2344E–07	1.7776E–07	6.8120E–08	7.8811E–07
2.25	0.660	5.1411E–05	6.7722E–07	1.6223E–05	6.7558E–06	5.6182E–08	1.6715E–06
2.5	0.678	1.1345E–04	4.7093E–06	5.3293E–05	2.4999E–05	6.1355E–08	2.3138E–06
3.0	0.730	7.3008E–05	−8.1538E–06	1.6524E–04	1.1935E–04	1.4861E–07	5.9637E–06
3.5	0.814	2.9970E–05	−2.0965E–05	1.2970E–04	1.2813E–04	1.6567E–07	1.3660E–05
	0.818	2.9463E–05	−1.9983E–05	1.2656E–04	1.2669E–04	1.6583E–07	1.3232E–05
4.0	0.852	1.5642E–04	−2.4338E–05	2.9263E–04	3.6171E–04	3.2160E–07	1.6469E–05
	0.860	1.5583E–04	−2.2444E–05	2.1669E–04	2.6593E–04	3.2216E–07	1.5292E–05
5.0	0.906	1.6303E–03	−1.9321E–04	7.9235E–04	8.8831E–04	2.3550E–05	3.6019E–05
	0.913	1.6274E–03	−1.9285E–04	7.8956E–04	8.8604E–04	2.3510E–05	3.5918E–05
6.0	0.978	4.4722E–04	−9.4674E–04	1.2512E–03	6.9065E–04	9.2737E–05	4.5324E–05
	0.986	4.4699E–04	−9.4558E–04	1.2149E–03	6.3286E–04	9.2700E–05	9.2700E–05

**Table 5.** Initial compositions (in mass fraction) used for the stellar models

Z	^{23}Na	^{24}Mg	^{25}Mg	^{26}Mg	^{26}Al	^{27}Al
0.02	3.818E−5	5.904E−4	7.750E−5	8.892E−5	0.0000E+00	6.642E−5
0.008	2.679E−5	4.143E−4	5.439E−5	6.240E−5	0.0000E+00	4.661E−5
0.004	1.393E−5	2.155E−4	2.829E−5	3.245E−5	0.0000E+00	2.424E−5

4.2 Results

In Figure 7 we plot the standard set of yields of ^{23}Na (upper left), ^{25}Mg (upper right), ^{26}Mg (lower left), and ^{26}Al (lower right) as a function of the stellar mass and composition. We weight the stellar yields by the three-component initial mass function (IMF) of Kroupa, Tout, & Gilmore (1993) given by the formula

$$\xi(m) = \begin{cases} 0 & \text{if } m < m_0, \\ a_1 \, m^{-1.3} & \text{if } m_0 < m \leq 0.5, \\ a_2 \, m^{-2.2} & \text{if } 0.5 < m \leq 1.0, \\ a_2 \, m^{-2.7} & \text{if } 1.0 < m < \infty, \end{cases} \quad (6)$$

where $\xi(m)dm$ is the probability that a star has a mass (in solar units) between m and $m + dm$. The constants are given by $a_1 = 0.29056$, $a_2 = 0.15571$, and $m_0 = 0.1\,\mathrm{M}_\odot$ (Hurley, Tout, & Pols 2002). In each figure, the black solid line (and points) refer to the $Z = 0.02$ models, the blue dashed line (and open squares) refer to the $Z = 0.008$ models, and the red dot-dashed line (and open circles) refer to the $Z = 0.004$ models. We plot for comparison the yields of Forestini & Charbonnel (1997, hereafter FC97), also weighted by the IMF. Along with the stellar yields, we also present the surface abundance results from some of our stellar models. In Figure 9 we present the time
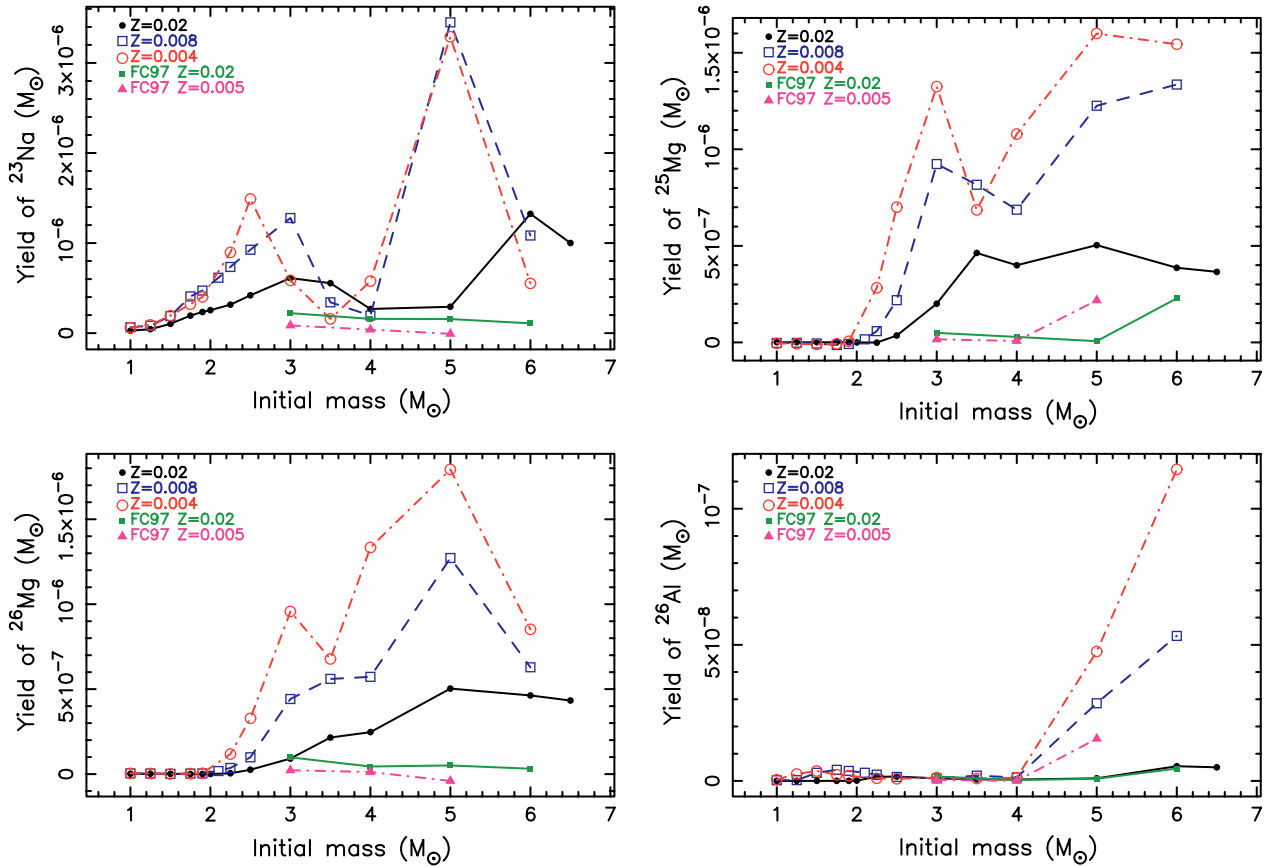
Figure 7 Weighted yield of ^{23}Na, ^{25}Mg, ^{26}Mg, and ^{26}Al as a function of the initial stellar mass (in M$_\odot$). See text for a description of the symbols.
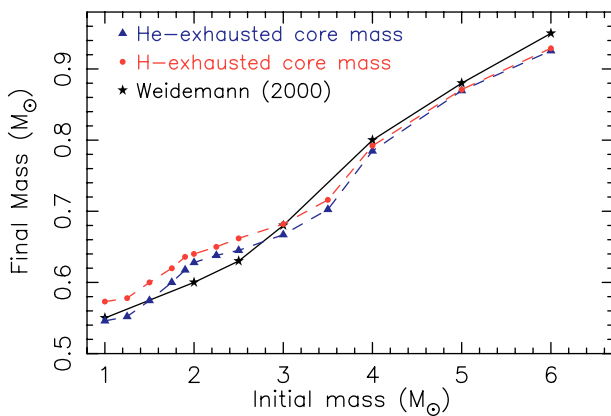

Figure 8 Initial–final mass relation from Weidemann (2000) plotted against the H-exhausted and He-exhausted core mass from the $Z = 0.02$ models.

variation of the relative proportions of the three Mg isotopes during the AGB evolution, and in Figure 10 we present the ^{26}Al/^{27}Al ratio for the same six models. In each figure, we show the results for the 4 M$_\odot$ (left) and 6 M$_\odot$ (right) models, with the $Z = 0.02$ models shown in the top panel, the $Z = 0.008$ models in the middle panel, and the $Z = 0.004$ models in the bottom panel.

Figure 7 shows that the yields produced from our models are strongly dependent on the initial metallicity. For all

species considered, the $Z = 0.004$ yields are considerably larger than the $Z = 0.02$ yields. The yields are also highly dependent on the initial stellar mass. As expected, low-mass models contribute little to the production of ^{25}Mg and ^{26}Mg. The intermediate mass models with $M \geq 4\,$M$_\odot$ produce the most ^{25}Mg and ^{26}Mg, as clearly demonstrated by Figure 9. For example, the 6 M$_\odot$, $Z = 0.004$ model (see bottom right panel of Figure 9) produces more ^{25}Mg and ^{26}Mg than any other. This is because HBB is very efficient at destroying ^{24}Mg, so that ^{25}Mg and ^{26}Mg account (in almost equal proportions) for all of the Mg in the envelope. Note also the large decrease in ^{25}Mg after HBB ceases; this is due to the continued dredge-up of material with more ^{26}Mg relative to ^{25}Mg (owing to the efficient destruction of ^{25}Mg in the H-shell ashes, as described in Section 3.2). The final yields reflect, however, the contribution from HBB: the ^{25}Mg yield is twice that of the ^{26}Mg yield.

The weighted ^{23}Na yield is bimodal, reflecting the contribution from the first dredge-up in low-mass models and HBB occurring in the most massive AGB models. Also as expected from Figure 10, the yields from the models with HBB produce the largest amount of ^{26}Al. We can see the effect of HBB on the 4 M$_\odot$ models. The 4M$_\odot$, $Z = 0.02$ model, which does not experience HBB, has a final ^{26}Al/^{27}Al ratio $\sim 6 \times 10^{-4}$ compared to the 4 M$_\odot$, $Z = 0.004$ model with HBB which has a final ^{26}Al/^{27}Al ratio $\sim 4 \times 10^{-3}$.
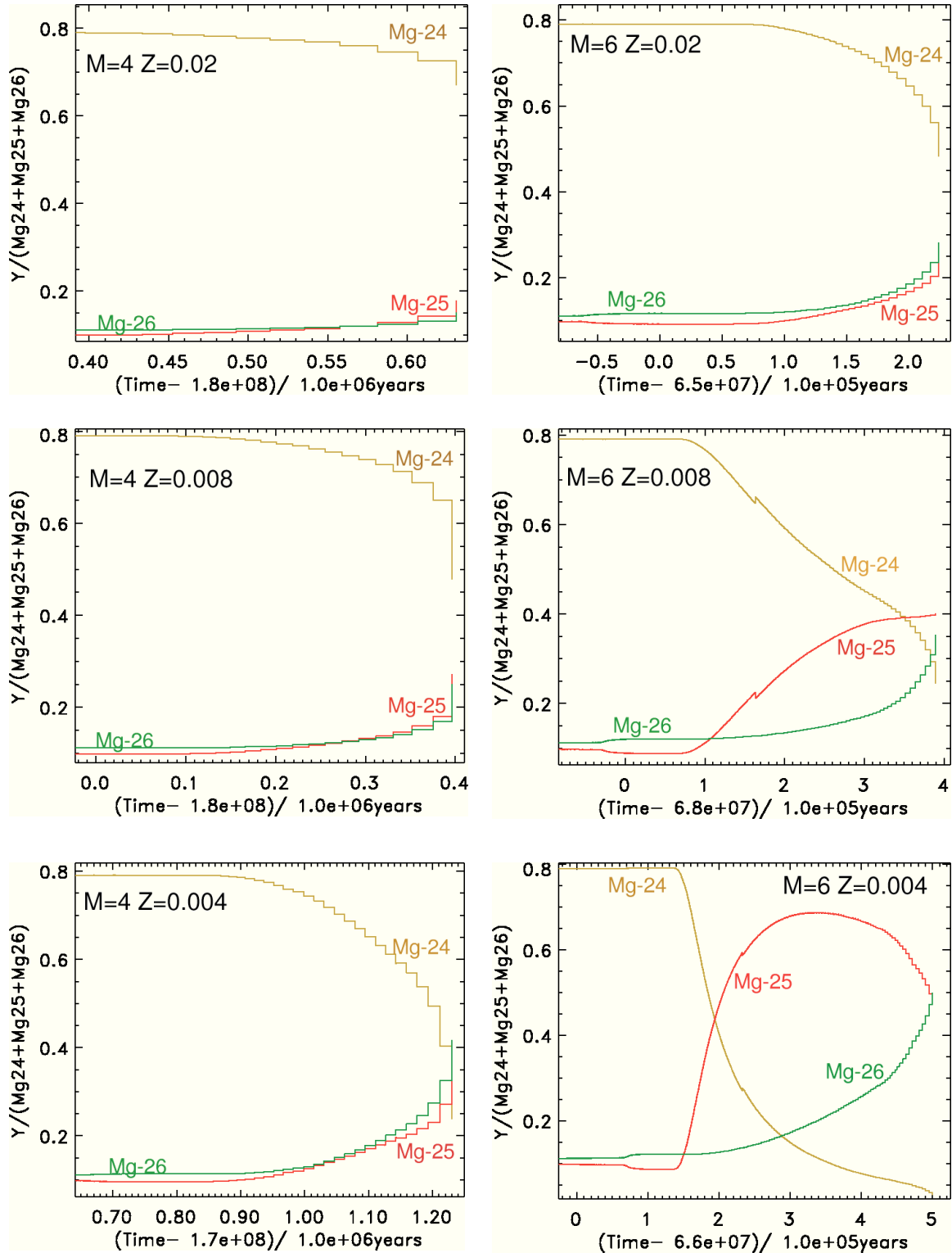
Figure 9 The abundance of ^{24}Mg, ^{25}Mg, and ^{26}Mg scaled to the total Mg abundance during the TP–AGB phase for the $4\,M_\odot$ and $6\,M_\odot$ models.

The difference between our standard set of stellar yields, plotted in Figure 7, and the set calculated with $\lambda = 0.3$ is small in most cases. This is especially true for the intermediate mass models which experience many thermal pulses and HBB during the TP–AGB phase, so the change to the surface composition from the few remaining pulses is small. The difference at the lower mass models ($M \lesssim 3\,M_\odot$) is more significant. There are two main reasons for this. The first reason is that lower mass models do not experience as many thermal pulses with TDU as do the higher mass models (as Table 2 shows). Secondly, owing to long interpulse periods ($>50\,000$ years), a considerable
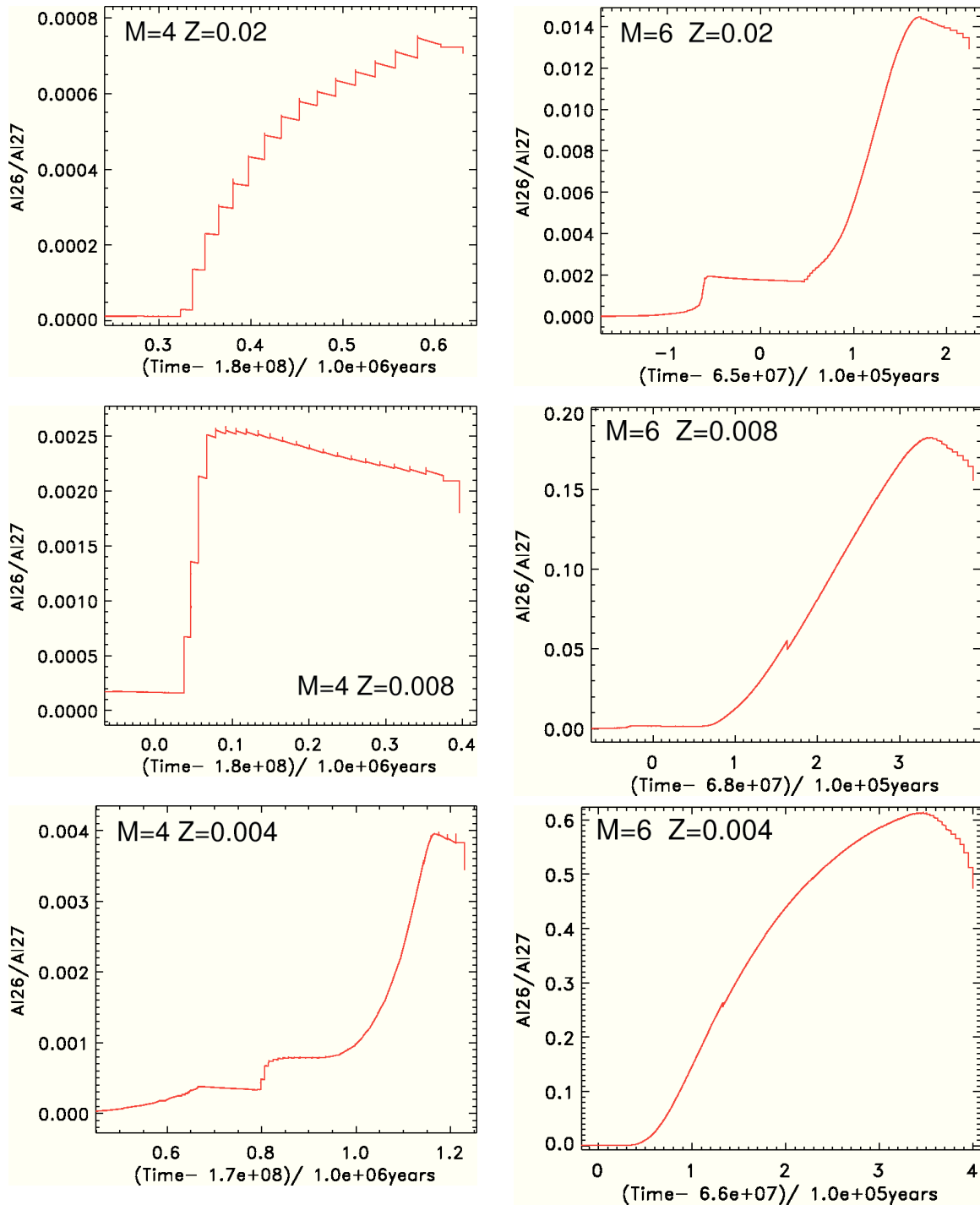
Figure 10 The time evolution of the ^{26}Al/^{27}Al ratio for the 4 M$_\odot$ and 6 M$_\odot$ models. The results for 5 M$_\odot$ are very similar in shape to the 6 M$_\odot$ cases, but with peaks of 0.002 ($Z = 0.02$), 0.07 ($Z = 0.008$), and 0.20 ($Z = 0.004$).

amount of matter may be lost between thermal pulses, which leads to a significant change to the stellar yield.

If we compare our results to FC97, we see from Figure 7 that we produce more ^{23}Na, ^{25}Mg, and ^{26}Mg at all masses and metallicities. We also produce more ^{26}Al in the $Z = 0.008$ and $Z = 0.004$ models but about the same at $Z = 0.02$. The large difference between our yields and those of FC97 is most likely explained by the different modelling approaches used. We use detailed

stellar models for most of the TP–AGB phase, only using synthetic modelling for the final few thermal pulses. In comparison, FC97 use detailed modelling for the pre-AGB phase and for a few thermal pulses. The majority of the thermal pulses were calculated synthetically. The surface abundance changes caused by HBB are highly dependent on the temperature (and the density) at the base of the convective envelope. If these quantities are not treated correctly in the synthetic model, the resulting

yields will be quite different to those found from detailed modelling. For example, FC97 extrapolated the behaviour of the temperature at the base of the envelope forward in time, realising that this extrapolation was likely to be incorrect.

The yields presented in Figure 7 are subject to many uncertainties including the modelling of convection, which determines if and when the TDU occurs. We note that many authors still do not find the TDU in AGB models without including some form of overshoot (see Mowlavi 1999a and Herwig 2000) beyond the base of the convective envelope. Herwig (2000) includes diffusive convective overshoot on all convective boundaries and obtains very efficient dredge-up. He also finds that the composition of the intershell is much different from standard models, where the ^{16}O and ^{12}C mass fractions are about 20% and 50% respectively (compared to 2% and 25% in standard models). The ^{22}Ne mass fraction found in Herwig's (2000) models are similar to ours, at about 2%, so in principal the Mg yields should be similar. However, the convective overshoot might change the temperature profile in the convective pocket, which would affect the rate of ^{25}Mg and ^{26}Mg production.

The uncertainty in the mass-loss rates applied during the AGB phase strongly affects the stellar yields. The Vassiliadis & Wood (1993) mass-loss formula that we use results in low mass-loss rates for most of the TP–AGB, and very high mass loss near the end of the AGB phase, where most of the convective envelope is lost in the last few thermal pulses. Figures 5, 6, 9, and 10 show that the largest changes to the surface abundance of the Mg isotopes occurs during the final few thermal pulses. The surface abundance of the isotopes altered by HBB, such as ^{23}Na and ^{26}Al, reach their peak value before the mass-loss rates become very high, so consequently the yields of these species would not be as affected by a different choice of mass-loss formula as would the yields of the Mg isotopes. However, the choice of a different mass-loss law might result in HBB being shut off at an earlier envelope mass or not occurring at all, which would drastically alter the surface abundance of the species effected by HBB.

There is further uncertainty in the stellar yields from some of the nuclear reaction rates involved in the Ne–Na and Mg–Al chains, and α-capture during He burning. Arnould et al. (1999) give a discussion of the uncertainties affecting the NACRE compilation of reaction rates, and how these uncertainties might affect the surface abundance calculations. Briefly, there are significant uncertainties in the rate of the ^{22}Ne(p,γ)^{23}Na reaction for temperatures over about 30×10^6 K. If the lower limit of the NACRE compilation is used, significantly less ^{23}Na will be produced from H burning. In the Mg–Al chain, there are large uncertainties in the ^{26}Mg(p,γ)^{27}Al reaction, and Arnould et al. (1999) comment that significant amounts of ^{27}Al could be produced if the NACRE upper limit is selected. We note also that the ^{26}Al(p,γ)^{27}Si reaction is uncertain by more than a factor of 10^3 at temperatures above 50×10^6 K. In regards to the ^{22}Ne

α-capture reactions, there are large uncertainties in the ^{22}Ne(α,n)^{25}Mg reaction at temperatures between 150 and 400×10^6 K (Arnould et al. 1999). If the NACRE lower limit of this rate, and the upper limit of the ^{22}Ne(α,γ)^{26}Mg reaction (though not as uncertain), is used, the stellar models might produce more ^{26}Mg relative to ^{25}Mg via He-shell burning.

4.3 Initial–Final Mass Relation

The final remnant masses used in the yield calculations are given in Table 3 for the $Z = 0.02$ models and Table 4 for the $Z = 0.008$ and $Z = 0.004$ models. The final remnant mass is chosen to be the mass of the H-exhausted core at the end of the evolution calculation, with the synthetic evolution included for the final pulses (where needed). There are two remnant masses for models that have the remaining thermal pulses calculated with synthetic evolution. The first remnant mass is from the calculation with λ taken from Table 2, and the second from the calculation with $\lambda = 0.3$. The second remnant mass is larger than the first, because a larger value of λ results in deeper TDU, which in turn results in a smaller core mass after a thermal pulse than the case with less efficient TDU. From here on, we refer to the first entry for each model as the final mass.

The final H-exhausted core mass depends upon a number of factors, including the mass-loss law chosen for the AGB phase, the occurrence and efficiency of the TDU, as well as on the details of the previous central He-burning phase (which determines the mass of the He core at the beginning of the TP–AGB phase). In Figure 8 we compare the final masses for the $Z = 0.02$ models with the initial–final mass relation given by Weidemann (2000). The agreement is quite good for models with $M \gtrsim 3\,M_\odot$ but less so for models with $M \lesssim 3\,M_\odot$. We note that this is the mass range where observations demand carbon stars which the models have trouble in producing. This is probably more evidence for our need to improve our understanding of dredge-up and its commencement. Deeper dredge-up will produce a smaller final mass than a similar case with shallow dredge-up (Weidemann 2000). Hence if deeper dredge-up is required to match the carbon star luminosity function in this mass range, then a lower final mass will result, as required by Figure 8. It is our educated guess that what is required is for the evolution to occur at slightly lower core masses, and thus terminate at lower core masses, with only a small effect on the yields. But a quantitative estimate is not possible at present.

5 Discussion

The most abundant isotope of magnesium is ^{24}Mg, produced in supernovae. However early generations of AGB stars should also produce substantial amounts of ^{25}Mg and ^{26}Mg. Hence within a stellar population, the relative ratios of these isotopes can indicate the importance of AGB star contributions to the stellar material. For example, the first stars to form from supernovae should contain pure ^{24}Mg (i.e. ^{24}Mg : ^{25}Mg : ^{26}Mg = 100 : 0 : 0) but the AGB stars from this population will return large amounts

of ^{25}Mg and ^{26}Mg, so that the next generation will be enriched in the heavy isotopes, and will show very different ratios. Note that many of our models return material with as much ^{25}Mg and/or ^{26}Mg as ^{24}Mg as shown in Figure 9. All calculations start with solar Mg ratios, but as the 4 M$_\odot$ sequence shows, the continued dredge-up of ^{25}Mg and ^{26}Mg increases the relative contributions by factors of two or three to ^{24}Mg : ^{25}Mg : ^{26}Mg $\sim 60 : 20 : 20$. In the case where HBB is effective then the destruction of ^{24}Mg enhances this effect. The 6 M$_\odot$ models show values as extreme as $\sim 30 : 40 : 20$ at $Z = 0.008$ and almost $0 : 50 : 50$ at $Z = 0.004$.

Yong et al. (2003) discuss the possibility of pollution from two previous generations of AGB stars to explain the non-solar Mg isotopic ratios observed in giant stars in the globular cluster NGC 6752. First, a $Z = 0$ population of intermediate mass AGB stars is required to increase the Mg isotopic ratio from almost pure ^{24}Mg to near solar values (i.e. ^{24}Mg : ^{25}Mg : ^{26}Mg $= 80 : 09 : 11$). Then a second generation of intermediate mass AGB stars with [Fe/H] ~ -1.6 is required to obtain the non-solar Mg ratios, which are enhanced in ^{25}Mg and ^{26}Mg. A further constraint is that most of the stars observed by Yong et al. (2003) have more ^{26}Mg relative to ^{25}Mg, which is not seen in most of our stellar models. A quantitative estimate of the pollution scenario discussed by Yong et al. (2003) requires a chemical evolution model, and can be performed with the yields presented here.

AGB stars have been suggested as the source of some of the short-lived nuclides present in the early solar system (Busso et al. 1999). For ^{26}Al this seems to require material with ^{26}Al/^{27}Al $\sim 5 \times 10^{-5}$ (Wasserburg et al. 1994). Note that this is after dilution with the interstellar medium: one infers a ratio of at least a few $\times 10^{-3}$ in the ejecta (Wasserburg et al. 1994). Figure 10 shows this ratio for the same six models as shown in Figure 9. We see that the required ratio is easily produced for models with HBB, such as the 4 M$_\odot$ model with $Z = 0.004$, or any of the 5 M$_\odot$ (not shown) or 6 M$_\odot$ models.

The ion-probe analysis of meteorites is providing us with information about pre-solar grains and hence providing strong constraints on nucleosynthesis models. Aluminium has been detected in oxide grains (which form in oxygen-rich atmospheres) and SiC grains (which form in carbon-rich atmospheres). Each provides a constraint for a different physical regime in the evolution of AGB stars, possibly representing different stars and/or evolutionary states. A recent discussion is found in Nollett et al. (2003).

Within the oxide grains, the highest inferred ^{26}Al/^{27}Al ratio is about 10^{-2} at the time of formation. Although this is easily achieved by our models, there is much more information provided by the grains which must also be considered, such as the oxygen isotope ratios. In the mainstream SiC grains, an ^{26}Al/^{27}Al ratio of about 10^{-3} is obtained in a carbon-rich environment, where C/O > 1 (Amari et al. 2001a, 2001b). This result would seem to rule out AGB stars with HBB as a suitable environment to form the mainstream SiC grains. Low mass AGB stars with extra mixing have been suggested instead. In these low mass AGB models, carbon dredge-up increases the C/O ratio > 1, and a slow extra mixing process (so the ^{12}C is not efficiently burnt to ^{14}N) produces some ^{26}Al (Nollett et al. 2003). A quantitative study and confrontation between our models and grain measurements will be the subject of a later paper, where Si isotopes and s-process nuclides must also be included.

References

Amari, S., Nittler, L. R., Zinner, E., Gallino, R., Lugaro, M. A., & Lewis, R. S. 2001a, ApJ, 546, 248

Amari, S., Nittler, L. R., Zinner, E., Lodders, K., & Lewis, R. S. 2001b, ApJ, 559, 463

Angulo, C., et al. (the NACRE Collaboration) 1999, NuPhA, 656, 3, http://pntpm.ulb.ac.be/nacre.htm

Arnould, M., Goriely, S., & Jorissen, A. 1999, A&A, 347, 542

Barmina, R., Girardi, L., & Chiosi, C. 2002, A&A, 385, 487

Boothroyd, A. I., Sackmann, I.-J., & Ahern, S. C. 1993, ApJ, 416, 762

Busso, M., Gallino, R., & Wasserburg, G. 1999, ARA&A, 37, 329

Caughlan, G. R., & Fowler, W. A. 1988, ADNDT, 40, 283

Chen, W., Gehrels, N., & Diehls, R. 1995, ApJ, 440, L57

Chieffi, A. Dominguez, I., Limongi, M., & Straniero, O. 2001, ApJ, 554, 1159

Chiosi, C., Bertelli, G., Meylan, G., & Ortolani, S. 1989, A&A, 219, 167

Denissenkov, P. A., & Weiss, A. 1996, A&A, 308, 773

Denissenkov, P. A., Da Costa, G. S., Norris, J. E., & Weiss, A. 1998, A&A, 333, 926

Fenner, Y., Gibson, B. K., Lee, H.-C., Karakas, A., Lattanzio, J. C., Chieffi, A., Limongi, M., & Yong, D. 2003, PASA, submitted

Forestini, M., & Charbonnel, C. 1997, A&AS, 123, 241 (FC97)

Forestini, M., Goriely, S., Jorissen, A., & Arnould, M. 1992, A&A, 261, 157

Frost, C. A., & Lattanzio, J. C. 1996, ApJ, 473, 383

Frost, C. A., Cannon, R. C., Lattanzio, J. C., Wood, P. R., & Forestini M. 1998, A&A, 332, L17

Gay, P. L., & Lambert, D. L. 2000, ApJ, 533, 260

Grevesse, N., Noels, A., & Sauval, A. J. 1992, in Proceedings of the First SOHO Workshop: Coronal Streams, Coronal Loops, and Coronal and Solar Wind Composition (ESA SP-348), 305

Herwig, F. 2000, A&A, 360, 952

Hurley, J. R., Tout, C. A., & Pols, O. R. 2002, MNRAS, 329, 897

Iben Jr, I. 1991, in Evolution of Stars: The Photospheric Abundance Connection, eds. G. Michaud, & A. V. Tutukov (Dordrecht: Kluwer Academic), 257

Iglesias, C. A., & Rogers, F. J. 1996, ApJ, 464, 943

Izzard, R. G., Tout, C. A., Karakas, A. I., & Pols, O. R. 2003, MNRAS, submitted

Jorissen, A., & Arnould, M. 1989, A&A, 221, 161

José, J., & Hernanz, M. 1998, ApJ, 494, 680

Karakas, A. I., Lattanzio, J. C., & Pols, O. R. 2002, PASA, 19, 515

Kroupa, P., Tout, C. A., & Gilmore, G. 1993, MNRAS, 262, 545

Lattanzio, J. C. 1986, ApJ, 311, 708

Lugaro, M. A. 1998, in Proceedings of the Fifth International Symposium on Nuclei in the Cosmos, eds. N. Prantzos & S. Harissopulos (France: Editions Frontiéres), 501

Lugaro, M. A. 2001, PhD Thesis, Monash University

Maeder, A. 1983, A&A, 120, 113

Marigo, P. 2001, A&A, 370, 194

Meynet, G. 1994, ApJS, 92, 441

Mowlavi, N. 1999a, A&A, 344, 617

Mowlavi, N. 1999b, A&A, 350, 73

Mowlavi, N., & Meynet, G. 2000, A&A, 361, 959

Nollett, K. M., Busso, M., & Wasserburg, G. J. 2003, ApJ, 582, 1036

Prantzos, N. 1993, ApJ, 405, L55

Prantzos, N. 1998, in The Hot Universe, Proceedings of IAU Symposium 188, eds. K. Koyama, S. Kitamoto, & M. Itoh (Dordrecht: Kluwer Academic), 31

Rolfs, C. E., & Rodney, W. S. 1988, Cauldrons in the Cosmos (Chicago: University of Chicago Press)

Russell, S. C., & Dopita, M. A. 1992, ApJ, 384, 508

Schaller, G., Schaerer, D., Meynet, G., & Maeder, A. 1992, A&AS, 96, 269

Shetrone, M. D. 1996, AJ, 112, 2639

Siess, L., Livio, M., & Lattanzio, J. C. 2002, ApJ, 570, 329

Straniero, O., Chieffi, A., Limongi, M., Busso, M., Gallino, R., & Arlandini, C. 1997, ApJ, 478, 332

Thielemann, F. K., Arnould, M., & Truran, J. W. 1991, in Advances of Nuclear Astrophysics, ed. E. Vangioni-Flam et al. (France: Editions Frontiéres), 525

Timmes, F. X., Woosley, S. E., & Weaver, T. A. 1995, ApJS, 98, 617

Travaglio, C., Randich, S., Galli, D., Lattanzio, J. C., Elliot, L. M., Forestini, M., & Ferrini, F. 2001, ApJ, 559, 909

Vassiliadis, E., & Wood, P. R. 1993, ApJ, 413, 641

Ventura, P., D'Antona, F., Mazzitelli, I., & Gratton, R. 2001, ApJ, 550, L65

Wasserburg, G. J., Busso, M., Gallino, R., & Raiteri, C. 1994, ApJ, 424, 412

Weidemann, V. 2000, A&A, 363, 647

Wood, P. R., & Zarro, D. M. 1981, ApJ, 248, 311

Woosley, S. E., Langer, N., & Weaver, T. A. 1995, ApJ, 448, 315

Yong, D., Grundahl, F., Lambert, D. L., Nissen, P. E., & Shetrone, M. D. 2003, A&A, 402, 985